Tri-Sectional Approximation of the Shortest Path to Long-Term Voltage Stability Boundary with Distributed Energy Resources

Dan Wu†, *Member, IEEE*, Bin Wang‡, *Senior Member, IEEE*, Franz-Erich Wolter⋆, and Le Xie⋆⋆, *Fellow, IEEE*

***Abstract*—Ensuring long-term voltage stability is critical for reliable operations of power grids. High share of distributed energy resources (DERs) can create complicated system operation modes that may invalidate the traditional long-term voltage stability analysis based on typical operation modes. To address this challenge, this paper investigates how to compute the shortest path to the voltage stability boundary in the DER aggregated load space with large dispersion. Instead of working in the Euclidean space, we establish the analysis and computations on the algebraic power flow manifold to better capture the curvature change of the shortest path along the direction of losing stability. A modified optimal control framework is presented for obtaining the ground-truth of the smooth shortest path on the manifold. To efficiently and accurately solve for the shortest path, we further leverage the geometric features of the power flow manifold and propose a tri-sectional approximation model that is scalable for large-scale systems. Several numerical examples, up to the 1354-bus system, with different DER penetration levels and high dimensional renewable power injection variations are evaluated. The simulation results demonstrate that the tri-sectional approximation achieves high accuracy and efficiency to approximate the shortest path to the voltage stability boundary.**

***Index Terms*—Long-term voltage stability, DER penetrated load, manifold distance, tri-sectional approximation**

I. Introduction

The long-term voltage stability analysis is studied based on algebraic power flow equations and usually aims at finding the heaviest loading condition, namely the maximum power transfer, that a power grid can supply without losing the system equilibrium point. A traditional method based on the continuation power flow (CPF) approach is commonly used and well-practiced in the power industry, which requires a pre-defined varying direction of the load and generation, and then keeps tracking the power balance equilibrium over changes [1]–[6]. The CPF approach can be applicable if such a varying direction can be available from empirical experience, which is true for traditional power grids since there are only very few typical operation modes in their annual operation [7]. Traditional methods for analyzing voltage stability should also work for renewable-rich power grids if most renewable output can be regulated or accurately predicted.

†: Lab for Information and Decision Systems, Massachusetts Institute of Technology, Cambridge, MA, USA, danwumit@mit.edu; ‡: Grid Planning and Analysis Center, National Renewable Energy Laboratory, Golden, CO, USA bin.wang@nrel.gov; ⋆: Department of Electrical Engineering and Computer Science, Leibniz University Hannover, Germany, few@gdv.uni-hannover.de; ⋆⋆: Department of Electrical and Computer Engineering, Taxes A&M University, College Station, TX, USA, le.xie@tamu.edu

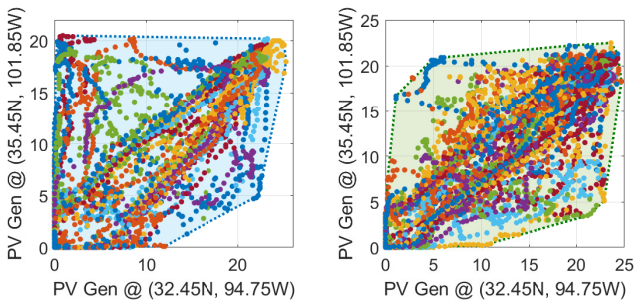

Fig. 1: Distributed Solar Generation (MW) at Two Locations in Texas (Left: Jan. 2006, Right: Jul. 2006)

Note: The x and y axes of Fig. 1(a) and 1(b) represent the PV generations at two locations in Texas. The wide dispersion of operating point dots in these two plots imply that the uncertainties from the renewable energy can bring in more operation modes to power grids, and introduce frequent switching among those modes.

The increasing penetration of variable renewable energy sources are diversifying power system operation modes with a larger space dispersion and forcing more frequent changes among these modes [7]. For example, Fig. 1 shows the distributed solar power generations at two different locations in Texas in 2006 [8]. The combinations of different generation modes clearly spanned into a large shaded area in the 2-D generation space. Needless to say the complexity of countlessly many modes in a higher dimensional distributed renewable generation space which can make a thorough analysis very difficult. This "burst of complexity" brings great challenges to the system planning [9], operation [7], protection [10], and control [11], [12]. It also introduces a great challenge to the CPF-based long-term voltage stability analysis because countlessly many possible directions need to be evaluated in a more frequent fashion to better address the drastically increased operation modes. This is true especially for power grids with significant amounts of unregulated DERs such as island power grids. For example, the total MW generation from unregulated residential rooftop solar in Maui grid is about 41% of the total load [13] and this number is still increasing [14]. In this case, traditional methods may not work well.

To address this challenge, alternative approaches based on the smallest voltage stability margin may help and deserves a revisit. The smallest voltage stability margin describes some type of distance from the current operation point to the worst

possible operation point. Although conservative in some cases, this margin provides a stability guarantee for renewable-rich power grids in a range of power varying directions. To construct such a distance, many indices reflecting the proximity to the voltage stability boundary were proposed [15]–[18]. A few common problems are noticed for these indices, for example, (i) their accuracy can be largely affected by system configurations and operating conditions [19], [20]; (ii) they may not satisfy the axioms of metric, resulting in a non-rigorous definition of distance and preventing voltage stability analysis based on metric space structures; and (iii) it is not clear how they relate to the margin in the power space, which is the most common practice in power industry [21], [22].

To find the smallest voltage stability margin in the power space, early work [23] proposed an optimization framework to solve for the smallest power injection margin from the current operating point to the voltage stability boundary. A simple and efficient iterative method computing the locally nearest point on the singular boundary in power space was developed in [24], [25], which was underpinned by the thorough and sophisticated analysis presented in [26]. Based on the optimization framework, recent progress has enabled the demand response technology to maximize the voltage stability margin [27], [28].

Only recently we realized that almost all the existing optimization-based approaches in the power space utilize the Euclidean metric to compute the smallest distance from the operating point to the stability boundary, disregarding the curvature change of the manifold spanned by the nonlinear power flow equations. The smallest Euclidean distance can provide an over-conservative voltage stability margin and a misleading worst power varying direction [29]. This led to our previous work [29] leveraged the Riemann metric and optimal control technique to search for the shortest manifold distance from the operating point to the voltage stability boundary. Compared to the shortest path with the Euclidean metric, the shortest path in the Riemann metric, as proved and demonstrated in [29], always ends on the correct piece [1] of the singular submanifold that contributes to the voltage instability. Still, the optimal control framework in [29] and the differential geometry techniques in [30]–[33] are computationally expensive, especially for large-scale power system applications.

The key contribution of this paper is the development of an efficient and accurate method to approximate the shortest path to the long-term voltage stability boundary on the manifold for large-scale applications. Detailed contributions are suggested as follows.

1) Based on the optimal control formulation in [29] for the long-term voltage stability problem, we propose a modified version considering the flexible DER aggregated load characteristic.
2) We propose an efficient model, named the *tri-sectional approximation*, to estimate the smooth shortest path to the voltage stability boundary on the algebraic power flow manifold.
3) We demonstrate the effectiveness of the proposed tri-sectional approximation: evaluated the accuracy by three proposed indices with direct physical interpretations, and achieve a speedup of $\times 1000$ compared to the method in [29] on different test systems with up to 1354 buses considering high dimensional renewable power injection variations.
4) We reveal that the shortest path to voltage instability may not be in the direction of a simultaneous decline of DER power generation. A combination of power generation increase and decrease at different DER aggregated buses can yield closer voltage instabilities.

The rest of the paper is organized as follows. Section II introduces the DER aggregated load model and the corresponding singularity condition. Section III summarizes the optimal control framework for computing the shortest path on the manifold. It will be used as the ground truth to evaluate the accuracy of our proposed method. Section IV introduces the proposed tri-sectional approximation model in detail. Section V defines three indices to evaluate the accuracy of the proposed tri-sectional approximation. Section VI presents five different numerical examples on large power systems with up to 1354 buses. Finally, Section VII concludes the paper.

II. Long-Term Voltage Instability Condition with DER Aggregated Load Characteristic

A. DER Aggregated Load Model in Quasi-Steady State

In this paper, we assume the ZIP load model as our load characteristic [34]. The impact of the ZIP load model on the PV-curve can be found in [35] The DER is integrated into the load feeder via grid-following or grid-forming technologies, in which the former one is adopted by almost all today's grid-connected inverters, and the later one is expected to play a bigger role in the near future [12]. In the quasi-steady state, we assume that the grid-following control scheme regulates the DER's output power, making it behave like a PQ source [12]. So the power balance equation at the load feeder is

$$\begin{aligned} P_f + jQ_f = (g_{ld} + jb_{ld})(V_d^2 + V_q^2) + (I_d - jI_q)(V_d + jV_q) \\ + (P_{ld,0} + jQ_{ld,0}) - (P_{der} + jQ_{der}) \end{aligned} \tag{1a}$$

$$P_{der}^{min} \le P_{der} \le P_{der}^{max} \tag{1b}$$

$$Q_{der}^{min} \le Q_{der} \le Q_{der}^{max} \tag{1c}$$

where $g_{ld} + jb_{ld}$ is the impedance component of the load; $I_d + jI_q$ is the current component of the load; $P_{ld,0} + jQ_{ld,0}$ is the power component of the load; and $P_{der} + jQ_{der}$ is the DER power injection within its limits.

Separating the active and reactive power from Eqn. (1a)

$$P_f = g_{ld}(V_d^2 + V_q^2) + I_d V_d + I_q V_q + P_{ld} \tag{2a}$$

$$Q_f = b_{ld}(V_d^2 + V_q^2) + I_d V_q - I_q V_d + Q_{ld} \tag{2b}$$

where we combine the power component of the ZIP load with the DER power injections into aggregated power variables $P_{ld} := P_{ld,0} - P_{der}$ and $Q_{ld} := Q_{ld,0} - Q_{der}$.

Although the DER aggregated load model can vary with time by any of its components, the following assumption is

[1]There could be multiple disconnected pieces of the singular submanifold while only one of them the system would encounter.

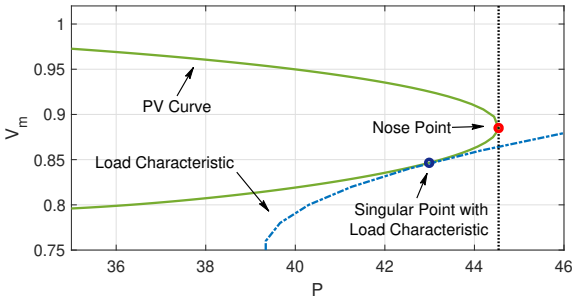

Fig. 2: Illustrative PV Curve, Nose Point, and Load Characteristic

adopted in this work to focus on DERs output variations by fixing the aggregated load, since a sudden change in load is usually not significant, e.g., at the transmission level: assuming that the renewable power generation in the DER can change much faster than the aggregated load fluctuations. Hence, g_{ld}, b_{ld}, I_d, I_q, $P_{ld,0}$ and $Q_{ld,0}$ are constant values, while only P_{der} and Q_{der} are time-varying variables. With this assumption, the power variation at each node totally depends on the DERs.

B. Singularity Condition with Load Characteristic

The singularity condition of the power flow Jacobian matrix is commonly used as an indicator of losing long-term voltage stability.

$$\text{PF}(V) - h = \mathbf{0} \tag{3a}$$

$$h = \begin{cases} h_{pq}(P_f, Q_f) & \text{for any PQ bus} \\ h_{pv}(P_g, V_m) & \text{for any PV bus} \\ h_{slack}(V_m, \theta_0) & \text{for any slack bus} \end{cases} \tag{3b}$$

$$\det\left(\frac{\partial \text{PF}}{\partial V}\right) = \mathbf{0} \tag{3c}$$

where Eqn. (3a)-(3b) are the standard power flow equations [interested readers may refer to Eqn. (3)-(6) of reference [36] for the detailed expressions], while Eqn. (3c) represents the singularity condition; V is the bus voltage vector that piles up the real part and the imaginary part; $\text{PF}(V)$ is the network-only power flow equation vector; vector h depends on the bus type, which specifies the active power injection P_f and reactive power injection Q_f at the PQ-bus, decides the active power injection P_g and voltage magnitude V_m at the PV-bus, and determines the voltage magnitude V_m and angle reference θ_0 at the slack bus for the standard power flow problem; Eqn. (3c) is the singularity condition of the Jacobian matrix with respect to bus voltage variables V.

To make Eqn. (3c) hold, the choice of P_g, P_f and Q_f needs to be carefully selected. This can be done by considering some P_g, P_f and Q_f as unknown variables and solve Eqn. (3) for these P_g, P_f, Q_f and the corresponding V.

The solution to Eqn. (3) is called the *nose point*, which is the furthest power injection point in the PV curve that admits a solution, shown as the red dot in Fig. 2. It suggests that as the nodal power injection increases further, the system will lose its equilibrium point beyond the nose point.

If more detailed load characteristics other than constant power at some nodes are to be considered, for example, our DER aggregated ZIP load model in Eqn. (2), then h_{pq} would depend on voltage V and the DER aggregated load power variables P_{ld} and Q_{ld}, as shown in Eqn. (4b). Then, the loss of equilibrium point may be postponed to the lower branch of the network PV curve, shown by the blue dotted curve in Fig. 2. Different static load models [37] and different compositions [35] can greatly change the location of the singular boundary. For example, if the constant power component occupies the majority of the load, the singular boundary is close to the nose point. On the other hand, if the load mainly comprises impedance, the singular boundary will be pushed further down in the lower branch of the PV-curve, which will eventually disappear at pure impedance load. Mathematically, the singular boundary should satisfy the following modified conditions.

$$\text{PF}(V) - h = \mathbf{0} \tag{4a}$$

$$h = \begin{cases} h_{pq}(V, P_{ld}, Q_{ld}) & \text{for any PQ bus} \\ h_{pv}(P_g, V_m) & \text{for any PV bus} \\ h_{slack}(V_m, \theta_0) & \text{for any slack bus} \end{cases} \tag{4b}$$

$$\det\left(\frac{\partial \text{PF}}{\partial V} - \frac{\partial h}{\partial V}\right) = \mathbf{0} \tag{4c}$$

where h_{pq} specifies the conditions for all PQ buses including load characteristics, e.g., Eqn. (2), in terms of bus voltages V and DER aggregated active and reactive power variables P_{ld} and Q_{ld}. This form of singularity condition (4c) and the DER aggregated load model (2) are applied throughout this paper.

III. The Shortest Path Model on Manifold in Optimal Control Framework

Searching for the shortest path on the algebraic power flow manifold can be computationally intensive. Prior work has developed differential geometric method for power flow computations on manifolds [33] which was based on prior research in computational differential geometry regarding geodesics in submanifolds and singularities of the geodesic exponential map [30]–[32], [38]. One theme of this paper is to develop an efficient method that can accurately approximate this kind of path. This method, called the *tri-sectional approximation*, will be introduced in detail in Section IV. To justify the appropriateness of the tri-sectional approximation, its results should be compared to the truly shortest path on the manifold, which motivates us to extend the optimal control framework developed in [29] to consider the DER aggregated load characteristic in (2).

Considering a connected power system with N_{bus} buses and N_{line} transmission lines. Let the PV bus index set be $\mathcal{G}_{pv}$, the PQ bus index set be $\mathcal{G}_{pq}$, the generator bus (PV and slack bus) index set be $\mathcal{G}_{gen}$, and the selected time-varying power injection bus index set be $\mathcal{G}_{var}$. Note that $\mathcal{G}_{var} \subseteq \mathcal{G}_{gen} \bigcup \mathcal{G}_{pq}$. The manifold distance model [2] in the

[2]In this paper, we define the distance in the power subspace. With this metric, a topology can be further defined in the power subspace which can be associated with the voltage subspace by inverting or unfolding the quadratic folding map between voltage and power.

optimal control framework [29] is written as follow.

$$\textbf{Minimize} \quad \int_0^1 \sqrt{\langle u(\tau), u(\tau)\rangle} d\tau \tag{5a}$$

$$\textbf{Subject to} \quad \frac{d}{d\tau} P_s(\tau) = u(\tau) \tag{5b}$$

$$\frac{d}{d\tau} V(\tau) = v(\tau) \tag{5c}$$

$$\frac{d}{d\tau} r(\tau) = \mathbf{0} \tag{5d}$$

$$f_{p,i}\big(V(\tau)\big) = P_{g,i} \tag{5e}$$

$$f_{v,i}\big(V(\tau)\big) = V_{g,i}^2 \tag{5f}$$

$$g_{p,k}\big(V(\tau)\big) = P_{f,k} \tag{5g}$$

$$g_{q,k}\big(V(\tau)\big) = Q_{f,k} \tag{5h}$$

$$h_{p,k}\big(V(\tau)\big) = P_{f,k} \tag{5i}$$

$$h_{q,k}\big(V(\tau)\big) = Q_{f,k} \tag{5j}$$

$$B\big(P_s(\tau), V(\tau)\big) \geq \mathbf{0} \tag{5k}$$

$$\begin{bmatrix} \partial f_{p,r}/\partial V \\ \partial f_{v,r}/\partial V \\ \partial (g_{p,k} - h_{p,k})/\partial V \\ \partial (g_{q,k} - h_{q,k})/\partial V \end{bmatrix}_{\tau=1}^{T} r(1) = \mathbf{0} \tag{5l}$$

$$\langle r(1), r(1)\rangle = 1 \tag{5m}$$

$$P_s(0) = P_s^0 \tag{5n}$$

$$V(0) = V^0 \tag{5o}$$

$$s \in \mathcal{G}_{var},\ i \in \mathcal{G}_{gen},\ k \in \mathcal{G}_{pq},\ r \in \mathcal{G}_{pv} \tag{5p}$$

where $u(\tau)$ and $v(\tau)$ are the control variable vectors that need to be solved in optimality. $P_s(\tau)$ includes all the selected time-varying nodal power injections. $V(\tau)$ is the bus voltage vector stacking the real part and the imaginary part into a single column. $r(\tau)$ is the auxiliary variable vector. $P_{g,i}$ is the active power injection at generator bus-i. It is a variable if $i \in \mathcal{G}_{var}$, or a constant otherwise. $V_{g,i}$ is the pre-specified voltage magnitude at generator bus-i. $P_{f,k}$ and $Q_{f,k}$ are the active and reactive power injection variables at PQ bus-k, including time-varying DER power injection if $k \in \mathcal{G}_{var}$. Since the focus of this paper is on the impact of DERs whose output variations are mainly from the active power, we evaluate the shortest path in the corresponding subspace of active power. There is no difficulty in combining other subspace into consideration, for example, active-reactive power subspace, or even voltage subspace.

Eqn. (5b)-(5d) are the dynamical equations of the optimal control system. Eqn. (5e) and (5f) are the active power balance equation and the voltage magnitude equation at generator bus-i. Eqn. (5g) and (5h) are the active and reactive power balance equations at PQ bus-k. Eqn. (5i) and (5j) are the load active and reactive power characteristics at PQ bus-k. Eqn. (5l) is the singularity condition. Eqn. (5k) includes all the engineering limits such as generator and DER power output limits. Eqn. (5m) is the end-time regularity condition. Eqn. (5n) and (5o) are the initial conditions for P_s and V.

The solution to the path-constrained optimal control model (5) represents the shortest path to the voltage stability boundary in the selected active power P_s-subspace. In this paper, the load characteristic functions (5i) and (5j) are specified by Eqn. (2a) and (2b).

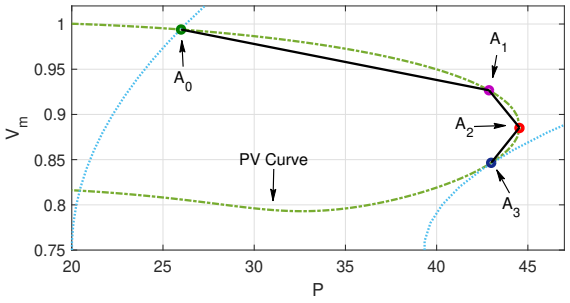

Fig. 3: Illustration of the Tri-Sectional Approximation from a Test System

IV. The Tri-Sectional Approximation Model

Solving the optimal control problem (5) for large-scale power systems is computationally very difficult. To tackle this challenge, we present a highly efficient and accurate approach, the tri-sectional approximation, to approximate the optimal solution of (5) in this section.

A. Geometric Interpretation

Before jumping into the symbolic description of the model, we first illustrate the geometry of this approach through a PV-curve plot in Fig. 3.

Suppose the system operates at point A_0 in Fig. 3 at the beginning. As the renewable power injection continuously declines in the DER, the aggregated load power demand increases equivalently, pushing the operating point moving along the green dash PV curve. The system will encounter voltage instability as the operating point reaches A_3 in Fig. 3. The arc between A_0 and A_3 (through A_2) is the path that needs to be approximated. The basic idea of the tri-sectional approximation is to use three concatenated line segments to approximate the arc between A_0 and A_3.

Due to the load characteristic, the singular point A_3 is on the lower branch of the PV curve, which implies that the nose point A_2 is between A_0 and A_3. Since the power flow equations are in the quadratic form, the nose point commonly has the largest scalar curvature in our interested range on the PV curve[3]. Thus, the nose point A_2 is considered as one of our concatenation points.

On the other hand, the curvature change from A_0 to A_2 can be substantial, which intrinsically shapes the shortest path in a nonlinear manner. Thus, we add another concatenation point A_1 between A_0 and A_2 to better accommodate the change of the scalar curvature. Therefore, the tri-sectional approximation is $\overrightarrow{A_0A_1} \oplus \overrightarrow{A_1A_2} \oplus \overrightarrow{A_2A_3}$.

Other choices of the number of concatenations have also been considered, for example, the bi-sectional approximation

[3]Empirically the nose point has the largest scalar curvature in its vicinity. It can be rigorously shown for the 2-bus system. Proving such a result for larger systems is one of our ongoing research topics.

and multiple sections. The bi-sectional approximation was very close to the traditional Euclidean distance, which can deviate away from the smooth shortest path on the manifold, yielding a very low accuracy. On the other hand, by using multiple sections (quad-section or more) we may achieve a better approximation accuracy, but the computational complexity will also be increased. This is because every time when we add a new intermediate point, a new set of voltage and power variables should be introduced to the formulated problem and a new set of power flow and singularity equations should be included as well. It expands the dimension of the optimization problem quickly for large-scale systems. Therefore, the tri-sectional approximation has been chosen in our work to achieve a reasonable approximation accuracy with the least computational complexity.

B. Tri-Sectional Approximation Model

Our objective is to find the smallest distance in the selected time-varying power injection space of this concatenated path $\overrightarrow{A_0A_1} \oplus \overrightarrow{A_1A_2} \oplus \overrightarrow{A_2A_3}$. Instead of converting the shortest path problem into the optimal control framework in the differential-algebraic form like (5), the tri-sectional approximation model can be formulated in a purely algebraic form.

$$\textbf{Minimize} \quad \sum_{j=1}^{3} \|P_{s,j} - P_{s,j-1}\| \tag{6a}$$

$$\textbf{Subject to} \quad f_{p,i,j}\big(V_j\big) = P_{g,i,j} \tag{6b}$$

$$f_{v,i,j}\big(V_j\big) = V_{g,i}^2 \tag{6c}$$

$$g_{p,k,j}\big(V_j\big) = P_{f,k,j} \tag{6d}$$

$$g_{q,k,j}\big(V_j\big) = Q_{f,k,j} \tag{6e}$$

$$h_{p,k,j}\big(V_j\big) = P_{f,k,j} \tag{6f}$$

$$h_{q,k,j}\big(V_j\big) = Q_{f,k,j} \tag{6g}$$

$$B_j(P_{s,j}, V_j) \geq \mathbf{0} \tag{6h}$$

$$\big(P_{s,1} - P_{s,0}\big)^T M_1 \big(P_{s,1} - P_{s,0}\big) = \gamma \tag{6i}$$

$$\begin{bmatrix} \partial f_{p,r,2}/\partial V_2 \\ \partial f_{v,r,2}/\partial V_2 \\ \partial g_{p,k,2}/\partial V_2 \\ \partial g_{q,k,2}/\partial V_2 \end{bmatrix}^T r_2 = \mathbf{0} \tag{6j}$$

$$\begin{bmatrix} \partial f_{p,r,3}/\partial V_3 \\ \partial f_{v,r,3}/\partial V_3 \\ \partial (g_{p,k,3} - h_{p,k,3})/\partial V_3 \\ \partial (g_{q,k,3} - h_{q,k,3})/\partial V_3 \end{bmatrix}^T r_3 = \mathbf{0} \tag{6k}$$

$$r_2^T r_2 = 1 \tag{6l}$$

$$r_3^T r_3 = 1 \tag{6m}$$

$$s \in \mathcal{G}_{var},\ i \in \mathcal{G}_{gen},\ k \in \mathcal{G}_{pq},\ r \in \mathcal{G}_{pv} \tag{6n}$$

$$j \in \{1, 2, 3\} \tag{6o}$$

where subscript j specifies the index of the concatenation point. $P_{s,j}$ includes all the selected time-varying power injection variables for the j-th concatenation point. V_j is the bus voltage vector stacking the real part and the imaginary part into a single column for the j-th concatenation point. $P_{g,i,j}$ is the active power injection at generator bus-i for the j-th concatenation point. It is a variable if $i \in \mathcal{G}_{var}$, or a constant otherwise. $V_{g,i,j}$ is the pre-specified voltage magnitude at generator bus-i for the j-th concatenation point. $P_{f,k,j}$ and $Q_{f,k,j}$ are the active and reactive power injection variables at PQ bus-k for the j-th concatenation point, including time-varying DER power injection if $k \in \mathcal{G}_{var}$. r_2 and r_3 are the auxiliary variable vectors for the second and third concatenation points.

Eqn. (6b) and (6c) are the active power balance equation and the voltage magnitude equation at generator bus-i for the j-th concatenation point. Eqn. (6d) and (6e) are the active and reactive power balance equations at PQ bus-k for the j-th concatenation point. Eqn. (6f) and (6g) are the load active and reactive power characteristics at PQ bus-k for the j-th concatenation point. Eqn. (6h) includes all the engineering limits such as generator and DER power output limits for the j-th concatenation point. Eqn. (6i) specifies the length of the first line segment $\overrightarrow{A_0A_1}$. Eqn. (6j) defines the nose point, which is the singularity condition when the constant power load is adopted [29]. Eqn. (6k) is the singularity condition considered in this paper with the more general ZIP load model, representing the voltage instability point. Eqn. (6l) and (6m) are the regularity conditions.

C. Determining the Length of the First Section

Note that in Eqn. (6i) we require the matrix $M_1 \succ 0$ and the scalar $\gamma = 1$. It creates a high dimensional ellipsoid whose intersection with the algebraic manifold confines the range of the first concatenation point, rendering a lower bound and an upper bound on the length of the first line segment $\overrightarrow{A_0A_1}$. This is necessary because, if we let the length of $\overrightarrow{A_0A_1}$ be arbitrary, the minimization process will send point A_1 either to A_0 or to A_2 for a shorter distance. This situation, however, results in a two-sectional path instead of a tri-sectional one.

In our numerical simulations, we choose M_1 to be a positive diagonal matrix for simplicity. Each entry on the diagonal of M_1 can be considered as the reciprocal of the square of the associated radius. The values of these radii can be selected through non-unique ways. One can choose $0.7\times$ the largest historical power injection value at each selected power varying bus in $\mathcal{G}_{var}$ as the radius. In our simulations, we first evaluate the loadability limit on each bus in $\mathcal{G}_{var}$ by CPF. The CPF procedure needs to be done only once for a given power system since the loadability limit is determined by the network topology and parameters. Then, set the radius as $0.7\times$ the associated loadability limit on that bus. The ratio 0.7 is selected from a heuristic observation that the Ricci curvature tensor [39] changes in a substantial way only when the operating point is approaching the nose point. Note that the Ricci curvature measures how the manifold deforms when we move along geodesic curves. So our observation implies that a relatively large secant length for the first section can achieve a good approximation accuracy.

Based on the heuristic selection of the radii, we may further improve the approximation performance by slightly scaling up γ beyond 1. It is equivalent to scaling up all the radii by a factor of $\sqrt{\gamma}$, expanding the linear approximation of the region in which Ricci curvatures remain small. As can be

seen later in Section VI, a slight increase of γ can improve the approximation performance in all three indices defined in Section V. There could be alternative ways to adjust γ. One way is to keep track of an index until it reaches the best performance. For example, $\cos\theta$ defined in Section V firstly increased and then decreased when γ kept increasing, shown in Table III, V and VII. Following this observation, we may choose γ when $\cos\theta$ reaches its maximum value. A small modification should be made here. Since we don't know the smooth shortest path in advance, we may consider the angle θ as the angle difference between the tri-sectional approximations of $\gamma = 1$ and γ at some other values. Another observation is that γ cannot be too large since extra large radii can make the ellipsoid un-intersect with the manifold, losing solvability. Based on this property, an alternative way to choose γ is to increase γ until the problem is infeasible or exhibits a solution jump.

D. Remarks on Numerical Solver and Solution

Problems (5) and (6) are both non-convex optimization problems. Generically, it is difficult to find the global minimum. For the illustration of multiple local minima, interested readers are referred to [29]. To numerically solve (5) and (6), IPOPT is adopted in this work. We don't expect IPOPT to always converge to the global optimum, because of the fact that IPOPT is a local solver for smooth optimization problems and the quality of the solution highly depends on selected initial conditions. On the other hand, even if IPOPT converges to the global optimum, currently there lacks an effective criterion to verify the global property.

Besides solving the global optimum, it is also practically meaningful to solve local optima based on certain predicted initial paths. For example, in power systems we can take the time series prediction of load and (DER) generation as the initial path condition. The locally minimal path based on the prediction informs system operators about the dangerous path that is more likely to happen, provided an adequate prediction. When IPOPT converges to such a local optimum of problem (6), the solution is still a very good tri-sectional approximation for the local minimal path on the manifold, as to be shown in Fig. 6, Fig. 8 and Fig. 10 in this paper. So, if we can live with local minimal path, local solvers have little influence on the quality of tri-sectional approximation.

V. Accuracy Evaluation

In the previous sections we presented both the exact model (5), defining the ground truth, and the proposed tri-sectional approximation model (6). Applying appropriate solvers to these models can yield their corresponding solutions.

Suppose the optimal solution to (5) is a differentiable path[4] $L(\tau) = \big(P_s^\star(\tau), V^\star(\tau)\big)$ for $\tau \in [0,1]$, shown as the green curve in Fig. 4. The optimal solution to (6) comprises three points $\big\{A_1, A_2, A_3 = \big\{(P_{s,1}^\star, V_1^\star), (P_{s,2}^\star, V_2^\star), (P_{s,3}^\star, V_3^\star)\big\}$, which forms the concatenated line segments in Fig. 4. To evaluate the accuracy of the proposed model (6), we need to evaluate how close $\overrightarrow{A_0A_1} \oplus \overrightarrow{A_1A_2} \oplus \overrightarrow{A_2A_3}$ is to $L(\tau)$.

[4]As we argued in [29], it only requires almost everywhere differentiable.

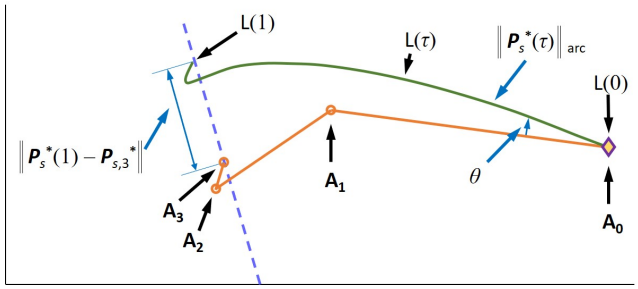

Fig. 4: Differentiable Path VS Tri-Sectional Approximation

A. Index 1: Directional Angle Difference at the Starting Point

Note that A_0 in Fig. 4 is given as the existing operating point which serves as the same starting point for both the optimal differentiable path and its tri-sectional approximation, namely, $L(0) = A_0$. At this point, we design the first index to evaluate the closeness between $L(\tau)$ and $\overrightarrow{A_0A_1} \oplus \overrightarrow{A_1A_2} \oplus \overrightarrow{A_2A_3}$: the directional angle difference. Specifically, consider

$$\cos\big(\theta\big) := \frac{\langle \frac{d}{d\tau}L(0), A_1 - A_0\rangle}{\|\frac{d}{d\tau}L(0)\|\ \|A_1 - A_0\|} \tag{7}$$

where θ is the angle from the tri-sectional approximation to the shortest path (shown in Fig. 4). The ideal target for this index is 1.0 (or 100%).

Physically speaking, the shortest path to the voltage instability boundary can reveal the critical direction in which the selected power variations can destabilize the system with the minimum effort. Our tri-sectional approximation should not deviate from this direction too much. Otherwise, the approximation may fail to provide a realistic warning in the sense of the most dangerous power varying direction.

B. Index 2: Power Difference Ratio at the Ending Point

The ending point of the shortest path to the voltage stability boundary reveals the closest singular point to the existing operating point. It can inform system operators about the most vulnerable future power injection plan associated with the current operating point. Having a decent estimation of this point is beneficial to the voltage stability control and system reliability assessment. Therefore, it is very relevant to understand the accuracy of our approximated closest singular point compared to the true closest singular point.

The index we designed to achieve this goal is based on the power difference at the ending points of $L(1)$ and A_3. Mathematically, we consider

$$\eta\% := \frac{\|P_s^\star(1) - P_{s,3}^\star\|}{\|P_s^\star(1)\|} \times 100\% \tag{8}$$

where $P_s^\star(1)$ is the selected time-varying power variable vector in the optimal path $L(\tau)$ at the ending time $\tau = 1$. $P_{s,3}^\star$ is the selected power variable vector at point A_3. The ideal target for this index is 0.

C. Index 3: Power Injection Distance Ratio

The arc length of the shortest path to the voltage stability boundary can be regarded as the smallest voltage stability

TABLE I: Numerical Example Settings

Settings	12case	39case1	39case2	1354case1	1354case2
Selected DER Bus	{5,7}	{4,9}	{8,20}	{309,393}	{42, 92, 160, 241, 453, 513, 1221}
Slack Bus	{10}	{31}	{31}	{640}	{640}
Load Model	0.3 Z 0.5 I 0.2 P	0.3 Z 0.5 I 0.2 P	0.3 Z 0.5 I 0.2 P	0.6 Z 0.2 I 0.2 P	0.6 Z 0.2 I 0.2 P
DER ratio*	60%	45%	34%	87%	53%

*DER ratio represents the local DER penetration level on the selected buses with variable power injections. This ratio is selected to ensure that the long-term voltage instability can happen by varying the DER power injections within their limits.

margin on the manifold associated with the current operating point. With this information, the system operator can determine if a future operating point is guaranteed to be stable in terms of the long-term voltage behavior.

Based on this interpretation of stability margin, the third index estimates the accuracy of the tri-sectional approximation by comparing the distance of the concatenated path to the manifold distance of the true shortest path in the selected power injection space.

$$d\% := \frac{\sum_{j=1}^{3} \|P^{\star}_{s,j} - P^{\star}_{s,j-1}\|}{\|P^{\star}_{s}(\tau)\|_{arc}} \times 100\% \tag{9}$$

where $\|P^{\star}_{s}(\tau)\|_{arc}$ is the arc length of $P^{\star}_{s}(\tau)$ from $\tau = 0$ to 1. Since the tri-sectional approximation is a truncated estimation of the real shortest path, its distance should be smaller than the manifold distance of the real shortest path, which implies that $d\% \leq 100\%$. The ideal target of this index is 100%.

VI. Numerical Simulations

In this section, we firstly demonstrate the accuracy of our proposed approximation in three examples: the 12-Bus system modified from the WSCC 9-Bus system [29] and two different scenarios of the IEEE 39-Bus system. Then, we show the scalability of the proposed method on two scenarios of the 1354-Bus PEGASE European high voltage transmission network system[5] [40], [41].

A summary of system settings are provided in Table I, in which the first and second rows specify the variable power injection space, and the third row specifies the ZIP load components ratios. These ratios are used to obtain the ZIP values of the load. For example, $(0.3Z, 0.5I, 0.2P)$ means that at the given operating point (the initial power injection) the impedance component $g_{ld} + jb_{ld}$ contributes 30% to the network power injection at each PQ bus; the current component $I_d + jI_q$ contributes the next 50%; and the aggregated power component $P_{ld}+jQ_{ld}$ in (2) contributes the rest 20%. The last row of Table I provides the DER penetration levels, ranging from 34% to 87%, which can induce voltage instability by varying DER power injections within their limits.

For comparison, we also compute the closest Euclidean distance in the vicinity of the shortest manifold path. The

[5]A permutation of the 1354-bus numbering set has been performed to better serve our data structure.

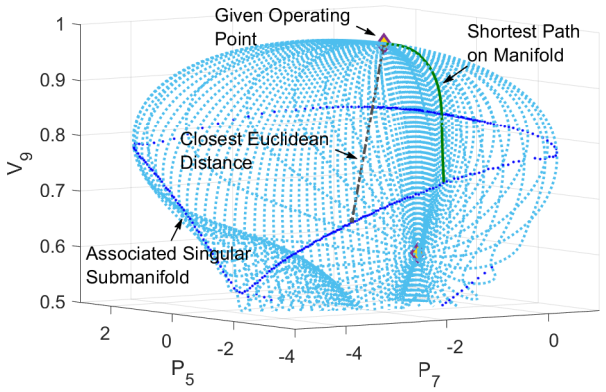

Fig. 5: 12-Bus System Global View

TABLE II: 12-Bus Case DER at Bus-5 and 7

Method	Initial P_{der}, pu	Final P_{der}, pu	Final P_{ld}, pu
Manifold	(1.02, 2.424)	(2.368, 0.375)	(1.168, -2.325)
Euclidean	(1.02, 2.424)	(0.211, 2.928)	(-0.989, 0.228)

Euclidean distance model is modified from the model in [27] to accommodate the DER aggregated ZIP load characteristics in Eqn (2). One should note that many local minimum Euclidean distances coexist in all the examples, and the smallest (maybe global) minima end on the non-associated (incorrect) piece of the singular submanifold, which yield serious misleading information about voltage stability margins and directions of losing stability. A comprehensive discussion of these issues, as well as using the manifold distance to avoid them, can be found in [29]. For reasonable comparisons in this paper, we chose the minimum Euclidean distance which is closest to the shortest path on the manifold, and ends on the associated (correct) piece of the singular submanifold.

Throughout this section, all the numerical simulations are performed in Matlab 2017 environment on a 64-bit personal computer with an Intel i7 2.8GHz CPU and 16GB RAM. The primal-dual interior-point solver "IPOPT" [42] is used for solving the the tri-sectional approximation model (6). The optimal control solver "ICLOCS2" [43]–[45] is used for solving the manifold distance model (5).

A. 12-Bus System

We present a global view of the algebraic power flow manifold for this particular example in the selected (P_5, P_7, V_9)-subspace in Fig. 5 by the light blue color.

With a high penetration of the DER into the load feeder, the aggregated load characteristic can behave like a provider, shown in Fig. 5 as the positive P_5 or P_7 areas[6]. However, when the DER power injection drops due to the intermittency of the renewable energy, it is equivalent to have an increase of the load demand, which may cause voltage problems.

The long-term voltage stability boundary (associated singular submanifold) is depicted in Fig. 5 by the dotted deep blue

[6]We define the power injection to be positive, and the power absorption to be negative.

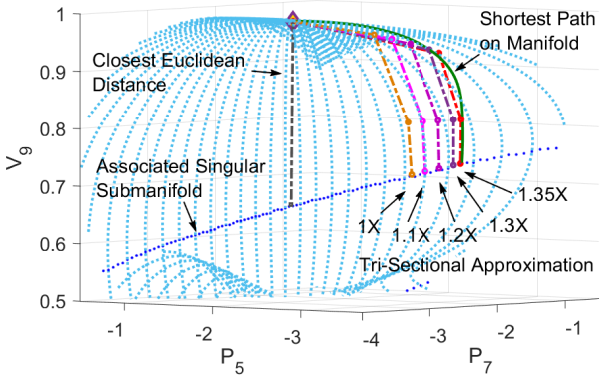

Fig. 6: 12-Bus System Local View

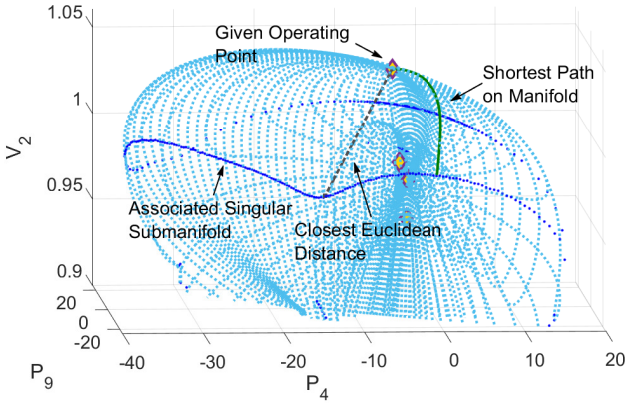

Fig. 7: 39-Bus System Scenario 1 Global View

TABLE III: Index Values for 12-Bus System

Model	Distance, pu power	$\cos(\theta)$	η %	d %
Manifold	3.0551	1	0 %	100 %
Euclidean	1.7966	0.5639	35.45 %	58.81 %
Tri-section 1x	2.9132	0.9766	19.18 %	95.36 %
Tri-section 1.1x	2.9175	0.9804	15.52 %	95.50 %
Tri-section 1.2x	2.9262	0.9817	12.02 %	95.78 %
Tri-section 1.3x	2.9394	0.9804	8.97 %	96.21 %
Tri-section 1.35x	2.9478	0.9788	7.82 %	96.49 %

TABLE IV: 39-Bus Scenario 1 DER at Bus 4 and 9

Method	Initial P_{der}, pu	Final P_{der}, pu	Final P_{ld}, pu
Manifold	(3, 1.187)	(0.812, 1.903)	(-3.188, -0.098)
Euclidean	(3, 1.187)	(2.691, 2.618)	(-1.309, 0.618)

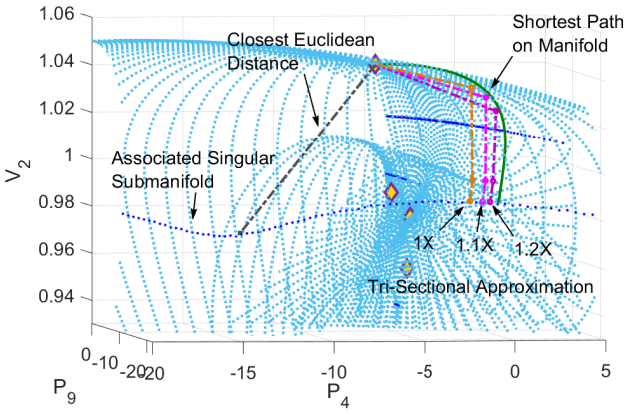

Fig. 8: 39-Bus System Scenario 1 Local View

curve. A decline of P_5 and P_7 can lead to a heavy loading condition with a very low voltage magnitude on Bus-9, shown by the "V" shape arc of the stability boundary.

By solving (5) we obtained the shortest path to the voltage stability boundary and plotted it by the smooth green curve on the manifold. It does not necessarily point to the most heavily loaded direction (the bottom of the "V" shape arc in Fig. 5). From Table II we can see that increasing $P_{der,5}$ and decreasing $P_{der,7}$ yield the shortest path on the manifold.

Table II indicates that decreasing $P_{der,5}$ and increasing $P_{der,7}$ yield the shortest Euclidean distance. These results suggest that a simultaneous decline of DER power injections at different buses may not be the direction of the shortest path towards voltage instability.

Fig. 6 shows a local view of the shortest path and its tri-sectional approximations solved from (6), depicted in warm colors based on different γ values from $\gamma = 1$ to 1.35. we can make a qualitative observation that the tri-sectional approximation can be very close to the shortest path on the manifold, provided an appropriate γ value[7]. To quantitatively evaluate how good our proposed approximation is, we computed the indices defined in Section V, and summarized the results in Table III. The indices verified that our proposed tri-sectional approximation model achieves high fidelity in the sense of all the proposed indices to approximate the shortest path on the manifold. On the contrary, the closest Euclidean distance, although happens to end on the correct singular submanifold in this case, deviates from the shortest path on the manifold in a substantial way.

[7]The value of γ determines the radii of the high-dimensional ellipsoid of Eqn. (6i).

B. 39-Bus System Scenario 1

The global view of the algebraic power flow manifold is shown in Fig. 7 in the selected (P_4, P_9, V_2)-subspace by the light blue color.

The moderate penetration of the DER into the aggregated load Bus-4 and Bus-9 can largely extend the feasible operation space of the system, as shown by the positive areas of P_4 or P_9. The long-term voltage stability boundary (associated singular submanifold) is depicted by the dotted deep blue curve. The shortest path on the manifold is shown by a deep green smooth curve. The closest Euclidean distance in the vicinity is plotted by the gray dash line segment.

Table IV suggests that decreasing $P_{der,4}$ and increasing $P_{der,9}$ yield the shortest path on the manifold. In contrast, reaching the closest Euclidean distance requires a slight decrease of $P_{der,4}$ and a large increase of $P_{der,9}$, which is quite different from the shortest path on the manifold.

In Fig. 8 three different tri-sectional approximations are plotted in warm colors based on different γ values from $\gamma = 1$

TABLE V: Index Values for 39-Bus System Scenario 1

Model	Distance, pu power	$\cos(\theta)$	η %	d %
Manifold	19.5736	1	0 %	100 %
Euclidean	14.9590	0.4397	50.75 %	76.42 %
Tri-section 1x	18.728	0.9921	5.51 %	95.68 %
Tri-section 1.1x	18.8735	0.9921	3.08 %	96.42 %
Tri-section 1.2x	19.0382	0.9894	1.63 %	97.26 %

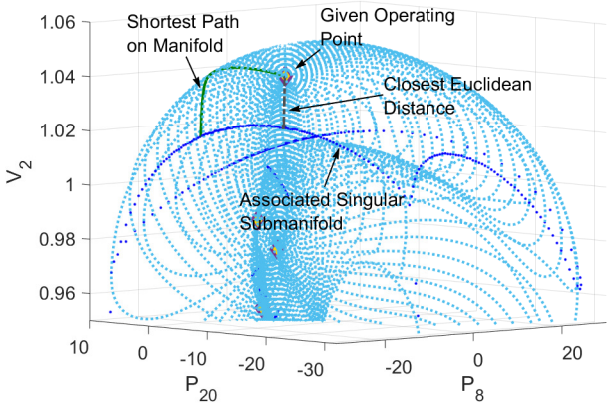

Fig. 9: 39-Bus System Scenario 2 Global View

TABLE VI: 39-Bus Scenario 2 DER at Bus 8 and 20

Method	Initial P_{der}, pu	Final P_{der}, pu	Final P_{ld}, pu
Manifold	(2.656, 3.640)	(2.281, 0.224)	(-2.219, -4.776)
Euclidean	(2.656, 3.640)	(3.273, 2.811)	(-1.227, -2.189)

to 1.2. From the plot we can make a qualitative observation that the proposed tri-sectional approximation is very close to the shortest path on the manifold, but not the closest Euclidean distance. To quantitatively verify our observation, we summarize all the indices in Table V. The results clearly show that the proposed tri-sectional approximation reaches a high accuracy in the sense of all the proposed indices, comparing to the closest Euclidean distance.

C. 39-Bus System Scenario 2

Fig. 9 shows the global view of the algebraic power flow manifold in the (P_8, P_{20}, V_2)-subspace by the light blue color. Again, the moderate DER penetration can extend the system operation space to the positive areas of P_8 or P_{20}. The heaviest loading condition happens when both DER injections decline, as shown by the sharp "V" arc of the stability boundary (associated singular submanifold).

However, from Table VI we can see that the shortest path on the manifold ends at the point where $P_{der,8}$ decreases slightly and $P_{der,20}$ reduces to almost zero. The closest Euclidean distance ends at the point where $P_{der,8}$ increases and $P_{der,20}$ decreases. The results again illustrate that a simultaneous decline of the DER power injections at different buses may not be the direction of the shortest path towards voltage instability.

Fig. 10 shows the local view of the three different tri-sectional approximations in warm colors for $\gamma = 1$ to 1.2. Again, we can make a qualitative observation that the proposed

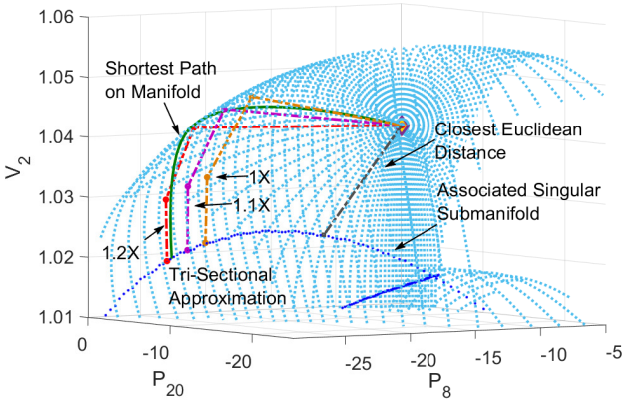

Fig. 10: 39-Bus System Scenario 2 Local View

TABLE VII: Index Values for 39-Bus System Scenario 2

Model	Distance, pu power	$\cos(\theta)$	η %	d %
Manifold	24.5266	1	0 %	100 %
Euclidean	14.6365	0.6347	34.00 %	59.68 %
Tri-section 1x	22.6930	0.9911	7.55 %	92.52 %
Tri-section 1.1x	23.0344	0.9940	3.53 %	93.92 %
Tri-section 1.2x	23.4273	0.9923	1.06 %	95.52 %

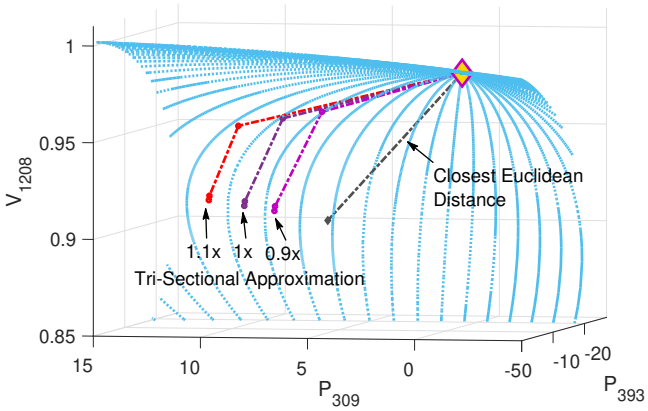

Fig. 11: 1354-Bus System Scenario 1

tri-sectional approximation model can be very close to the shortest path on the manifold. Quantitative results are summarized in Table VII, which further verify that the proposed tri-sectional approximation reaches a higher accuracy than the closest Euclidean distance in the sense of all the proposed indices.

D. 1354-Bus System Scenario 1

In this example, we are no longer able to solve the shortest path on the manifold by the optimal control framework (5) since no existing optimal control solvers can handle such a large-scale problem. Furthermore, evaluating the associated singular submanifold is extremely time-consuming so that we cannot display it as well. But we can still visualize the projection of the algebraic power flow manifold in Fig. 11. The tri-sectional approximations and the closest Euclidean distance are also plotted in Fig. 11. The difference

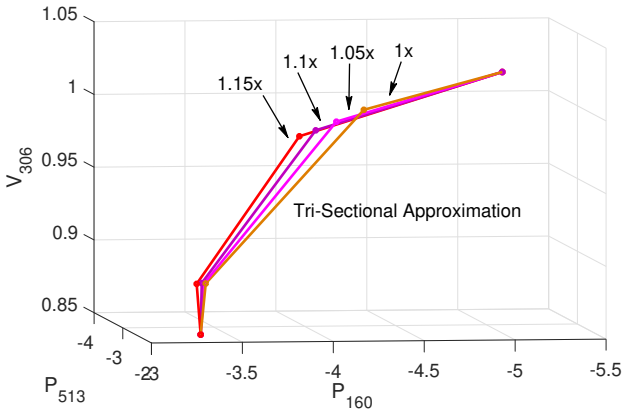

Fig. 12: 1354-Bus System Scenario 2

of ending-point power injections between the tri-sectional approximation $1.1\times$ case and the closest Euclidean distance is $(5.702, -1.040, -5.12)$ at the base power of 100 MVA.

E. 1354-Bus System Scenario 2

Previous examples are selected for 2-D algebraic power flow manifolds that allow good visualizations. The tri-sectional approximation model (6) is not limited to low-dimensional manifolds. In this subsection, we jump into a high-dimensional scenario on the same 1354-Bus system to show this capability. Specifically, our selected bus index set for the time-varying power variables is $\mathcal{G}_{var} = \{42, 92, 160, 241, 453, 513, 640, 1221\}$. The goal is to identify the shortest path from the given operating point to the voltage stability boundary in the $(P_{42}, P_{92}, P_{160}, P_{241}, P_{453}, P_{513}, P_{640}, P_{1221})$-subspace. Note that we are no longer able to show any visualization results of this manifold due to the high dimensionality. Only the tri-sectional approximations are depicted by projecting to a lower-dimensional power injection space in Fig. 12.

F. Computational Efficiency

In this subsection, we demonstrate the efficiency of solving the proposed tri-sectional approximation model (6) by comparing it to solving the optimal control model (5).

It should be noted that the computational time for both models can vary depending on different solvers, initializations, etc. To reduce the influence from these factors, we set the optimal control solver "ICLOCS2" to call "IPOPT" at the bottom level, which standardizes the internal solver for both models, and evenly choose 15 different initializations for each case to test on. The execution time is shown by the box-plot in Fig. 13, revealing the variance from different initializations. Since the 1354-Bus system is too large to solve in the optimal control framework, we can only present the execution time for the 12-Bus system and the 39-Bus system for the optimal control model (5).

From Fig. 13 we may reach a qualitative conclusion that solving the tri-sectional approximation model (6) can be much more efficient (several orders of magnitude lower) than solving

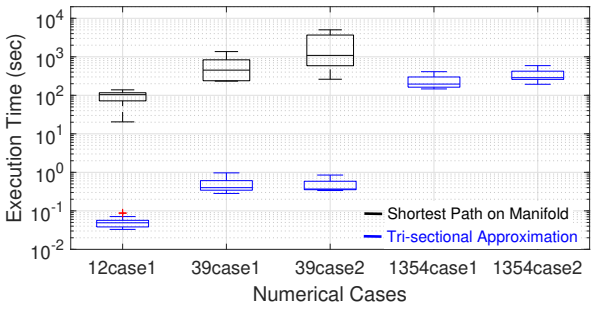

Fig. 13: Execution Time for All Cases

TABLE VIII: Execution Time for All Cases

Time (sec)	12case	39case1	39case2	1354case1	1354case2
Manifold	92.539	595.602	1951.621	-	-
Tri-Section	0.052	0.491	0.468	240.428	343.006
Speedup	1768×	1213×	4169×	-	-

the optimal control model (5) with smaller variances from different initializations. An average execution time comparison is provided in Table VIII, showing at least thousands of times faster when solving the proposed tri-sectional approximation model.

VII. Concluding Remarks

This paper discussed about how to search for the shortest path to the long-term voltage stability boundary for the more frequently changing modes of the future power grid with the DER aggregated load characteristic. Instead of searching in the Euclidean space with the Euclidean metric, we established the path computations on the algebraic power flow manifold with the Riemann metric to respect the curvature change of the system equilibrium trajectory in the quasi-steady state. A modified optimal control framework was presented considering DER aggregated load, serving as the true shortest path calculation on the manifold. By leveraging the geometric features of the power flow manifold, a tri-sectional approximation model was further proposed to approximate the true shortest path efficiently, leading to $\times 1000$ speedup. To demonstrate the accuracy of the tri-sectional approximation result, three indices with physical interpretations were proposed. Several numerical examples were tested and visualized for both qualitative observations and quantitative analysis. The high accuracy of the proposed tri-sectional approximation model was validated through the three indices on these examples. The computational efficiency and scalability of the tri-sectional approximation were further demonstrated on the 1354-bus system with high dimensional renewable power injection variations. An interesting observation suggested that a simultaneous decline of DER generations at different buses may not render the shortest path to the voltage collapse.

Although in this paper the tri-sectional approximation is found to be a good trade-off between speed and accuracy using today's technologies for solving the manifold distance, it is possible that the choice of a different number of concatenations may become better when the computing power and the

accuracy requirement evolve over time.

A promising future research direction can be investigating how the voltage-droop control [46] and the grid-forming technologies [12] in renewable power generation and DERs influence the long-term voltage stability boundary on the algebraic power flow manifold. It is also very intriguing to study the differences between the grid-following and the grid-forming technologies in terms of voltage stability analysis. The answers to these questions can help system planners and operators better configure the best combinations of different power electronics control schemes for future carbon-neutral power grids.

ACKNOWLEDGMENT

This work was supported in part by a MISTI MIT-Germany seed grant, in part by the DFG under Projektnummer 153232726 "Differential geometric Methods for analysing non-linear electrical circuits and their visualisation", in part by the U.S. Department of Energy's Office of Energy Efficiency and Renewable Energy (EERE) through the Solar Energy Technologies Office (SETO) under Grant DE-EE0009031, and in part by the National Science Foundation under Grant ECCS-2035688. It was co-authored by the National Renewable Energy Laboratory, operated by Alliance for Sustainable Energy, LLC, for the U.S. DOE under Contract No. DE-AC36-08GO28308. The views expressed in the article do not necessarily represent the views of the DOE or the U.S. Government. The U.S. Government retains and the publisher, by accepting the article for publication, acknowledges that the U.S. Government retains a nonexclusive, paid-up, irrevocable, worldwide license to publish or reproduce the published form of this work, or allow others to do so, for U.S. Government purposes.

REFERENCES

[1] K. Iba, H. Suzuki, M. Egawa, and T. Watanabe, "Calculation of critical loading condition with nose curve using homotopy continuation method," *IEEE Trans. on Power Syst.*, vol. 6, no. 2, pp. 584–593, 1991.

[2] H.-D. Chiang, A. J. Flueck, K. S. Shah, and N. Balu, "Cpflow: A practical tool for tracing power system steady-state stationary behavior due to load and generation variations," *IEEE Transactions on Power Systems*, vol. 10, no. 2, pp. 623–634, 1995.

[3] K. Chen, A. Hussein, M. Bradley, and H. Wan, "A performance-index guided continuation method for fast computation of saddle-node bifurcation in power systems," *IEEE Transactions on Power Systems*, vol. 18, no. 2, pp. 753–760, 2003.

[4] X.-P. Zhang, P. Ju, and E. Handschin, "Continuation three-phase power flow: a tool for voltage stability analysis of unbalanced three-phase power systems," *IEEE Transactions on Power Systems*, vol. 20, no. 3, pp. 1320–1329, 2005.

[5] S.-H. Li and H.-D. Chiang, "Continuation power flow with nonlinear power injection variations: A piecewise linear approximation," *IEEE Transactions on Power Systems*, vol. 23, no. 4, pp. 1637–1643, 2008.

[6] S. G. Ghiocel and J. H. Chow, "A power flow method using a new bus type for computing steady-state voltage stability margins," *IEEE Transactions on Power Systems*, vol. 29, no. 2, pp. 958–965, 2013.

[7] Q. Hou, E. Du, N. Zhang, and C. Kang, "Impact of high renewable penetration on the power system operation mode: A data-driven approach," *IEEE Transactions on Power Systems*, vol. 35, no. 1, pp. 731–741, 2020.

[8] Y. Zhang, "Solar power data for integration studies." [Online]. Available, https://www.nrel.gov/grid/solar-power-data.html.

[9] J. Bebic, "Power system planning: Emerging practices suitable for evaluating the impact of high-penetration photovoltaics," *NREL Technical Report NREL/SR-581-42297*, 2008.

[10] R. Seguin, J. Woyak, D. Costyk, J. Hambrick, and B. Mather, "High-penetration pv integration handbook for distribution engineers," *NREL Technical Report NREL/TP-5D00-63114*, 2016.

[11] A. Bernstein, "Final report for arpa-e nodes "real-time optimization and control of next-generation distribution infrastructure" project," *NREL Technical Report NREL/TP-5D00-78531*, 2021.

[12] Y. Lin, J. H. Eto, and et al, "Research roadmap on grid-forming inverters," *NREL Technical Report NREL/TP-5D00-73476*, 2020.

[13] R. W. Kenyon, B. Wang, A. Hoke, J. Tan, C. Antonio, and B. M. Hodge, "Validation of maui pscad model: Motivation, methodology, and lessons learned," in *52nd North American Power Symposium (NAPS)*, 2021.

[14] The Maui News, "29% of homes in maui county have installed rooftop solar." [Online]. Available, https://www.mauinews.com/news/local-news/2021/02/29-of-homes-in-maui-county-have-installed-rooftop-solar/.

[15] P. Kessel and H. Glavitsch, "Estimating the voltage stability of a power system," *IEEE Trans. Power Del.*, vol. 1, no. 3, pp. 346–354, 1986.

[16] I. Musirin and T. A. Rahman, "Novel fast voltage stability index (fvsi) for voltage stability analysis in power transmission system," in *Student Conference on Research and Development*, pp. 265–268, IEEE, 2002.

[17] J. W. Simpson-Porco and F. Bullo, "Distributed monitoring of voltage collapse sensitivity indices," *IEEE Transactions on Smart Grid*, vol. 7, no. 4, pp. 1979–1988, 2016.

[18] M. Kamel, A. A. Karrar, and A. H. Eltom, "Development and application of a new voltage stability index for on-line monitoring and shedding," *IEEE Trans. Power Syst.*, vol. 33, no. 2, pp. 1231–1241, 2017.

[19] C. A. Canizares, A. C. De Souza, and V. H. Quintana, "Comparison of performance indices for detection of proximity to voltage collapse," *IEEE Transactions on Power Systems*, vol. 11, no. 3, pp. 1441–1450, 1996.

[20] A. Chandra, A. K. Pradhan, and A. K. Sinha, "A comparative study of voltage stability indices used for power system operation," in *21st Century Energy Needs-Materials, Systems and Applications*, pp. 1–4, 2016.

[21] PowerWorld, "Steady-state power system security analysis with powerworld simulator." [Online]. Available, https://www.powerworld.com/files/S05AvailableTransferCapability.pdf.

[22] PJM, "Data miner 2." [Online]. Available, https://dataminer2.pjm.com/feed/transfer_limits_and_flows/definition.

[23] T. Jung, K. Kim, and F. Alvarado, "A marginal analysis of the voltage stability with load variations," in *Power Systems Computation Conference*, 1990.

[24] I. Dobson and L. Lu, "New methods for computing a closest saddle node bifurcation and worst case load power margin for voltage collapse," *IEEE Transactions on Power Systems*, vol. 8, no. 3, pp. 905–913, 1993.

[25] F. Alvarado, I. Dobson, and Y. Hu, "Computation of closest bifurcations in power systems," *IEEE Transactions on Power Systems*, vol. 9, no. 2, pp. 918–928, 1994.

[26] I. Dobson, "Computing a closest bifurcation instability in multidimensional parameter space," *Journal of nonlinear science*, vol. 3, no. 1, pp. 307–327, 1993.

[27] M. Yao, I. A. Hiskens, and J. L. Mathieu, "Improving power system voltage stability by using demand response to maximize the distance to the closest saddle-node bifurcation," in *2018 IEEE Conference on Decision and Control (CDC)*, pp. 2390–2395, IEEE, 2018.

[28] M. Yao, D. K. Molzahn, and J. L. Mathieu, "An optimal power-flow approach to improve power system voltage stability using demand response," *IEEE Transactions on Control of Network Systems*, vol. 6, no. 3, pp. 1015–1025, 2019.

[29] D. Wu, F.-E. Wolter, B. Wang, and L. Xie, "Searching for the shortest path to voltage instability boundary: From euclidean space to algebraic manifold," *International Journal of Electrical Power & Energy Systems*, vol. 131, p. 107127, 2021.

[30] F.-E. Wolter, P. Blanke, H. Thielhelm, and A. Vais, "Computational differential geometry contributions of thewelfenlab to grk 615," in *modelling, simulation and software concepts for scientific-technological problems*, pp. 211–235, Springer, 2011.

[31] M. Gutschke, A. Vais, and F.-E. Wolter, "Differential geometric methods for examining the dynamics of slow-fast vector fields," *The Visual Computer*, vol. 31, no. 2, pp. 169–186, 2015.

[32] H. Thielhelm, A. Vais, and F.-E. Wolter, "Geodesic bifurcation on smooth surfaces," *The Visual Computer*, vol. 31, no. 2, pp. 187–204, 2015.

[33] F.-E. Wolter and B. Berger, "Differential geometric foundations for power flow computations," *arXiv preprint arXiv:1903.11131*, 2019.

[34] A. Arif, Z. Wang, J. Wang, B. Mather, H. Bashualdo, and D. Zhao, "Load modeling - a review," *IEEE Transactions on Smart Grid*, vol. 9, no. 6, pp. 5986–5999, 2017.
[35] H. Li, H.-D. Chiang, H. Yoshida, Y. Fukuyama, and Y. Nakanishi, "The generation of zip-v curves for tracing power system steady state stationary behavior due to load and generation variations," in *1999 IEEE Power Engineering Society Summer Meeting. Conference Proceedings (Cat. No. 99CH36364)*, vol. 2, pp. 647–651, IEEE, 1999.
[36] D. Wu and B. Wang, "Holomorphic embedding based continuation method for identifying multiple power flow solutions," *IEEE Access*, vol. 7, pp. 86843–86853, 2019.
[37] V. Ajjarapu and S. Battula, "Effect of load modeling on steady state voltage stability," in *Electric Machines & Power Systems*, vol. 5, pp. 501–514, 1995.
[38] H. Thielhelm, A. Vais, D. Brandes, and F.-E. Wolter, "Connecting geodesics on smooth surfaces," *The visual computer*, vol. 28, no. 6, pp. 529–539, 2012.
[39] J. M. Lee, *Introduction to Riemannian manifolds*. Springer, 2018.
[40] S. Fliscounakis, P. Panciatici, F. Capitanescu, and L. Wehenkel, "Contingency ranking with respect to overloads in very large power systems taking into account uncertainty, preventive, and corrective actions," *IEEE Transactions on Power Systems*, vol. 28, no. 4, pp. 4909–4917, 2013.
[41] C. Josz, S. Fliscounakis, J. Maeght, and P. Panciatici, "Ac power flow data in matpower and qcqp format: itesla, rte snapshots, and pegase," *arXiv preprint arXiv:1603.01533*, 2016.
[42] A. Wächter and L. T. Biegler, "On the implementation of an interior-point filter line-search algorithm for large-scale nonlinear programming," *Mathematical programming*, vol. 106, no. 1, pp. 25–57, 2006.
[43] Y. Nie, O. Faqir, and E. C. Kerrigan, "Iclocs2: Try this optimal control problem solver before you try the rest," in *UKACC 12th International Conference on Control*, pp. 336–336, 2018.
[44] Y. Nie and E. C. Kerrigan, "Efficient and more accurate representation of solution trajectories in numerical optimal control," *IEEE Control Systems Letters*, vol. 4, no. 1, pp. 61–66, 2019.
[45] Y. Nie and E. C. Kerrigan, "External constraint handling for solving optimal control problems with simultaneous approaches and interior point methods," *IEEE Control Systems Letters*, vol. 4, no. 1, pp. 7–12, 2019.
[46] J. Weber, "Detailed documentation of software implementation of voltage droop with deadband in power flow calculation." [Online]. Available, https://www.powerworld.com/files/VoltageDroopControl_Software_Implementation.pdf.